Scanning metallic nanosphere microscopy for vectorial profiling of optical focal spots

Hui Yi,[1] Jing Long,[1] Hongquan Li,[1,2] Xiaolong He,[1] and Tian Yang[1,*]

[1]*University of Michigan - Shanghai Jiao Tong University Joint Institute, State Key Laboratory of Advanced Optical Communication Systems and Networks, Key Laboratory for Thin Film and Microfabrication of the Ministry of Education, Shanghai Jiao Tong University, Shanghai 200240, China*

[2]*Currently with Department of Electrical Engineering, Stanford University, Stanford, California 94305, USA*

[*]*tianyang@sjtu.edu.cn*

Abstract: Recent years have witnessed fast progress in the development of spatially variant states of polarization under high numerical aperture focusing, and intensive exploration of their applications. We report a vectorial, broadband, high contrast and subwavelength resolution method for focal spot profiling. In this experiment, a 100 nm diameter gold nanosphere on a silica aerogel substrate is raster scanned across the focal spots, and the orthogonal polarization components can be obtained simultaneously by measuring the scattering far field in a confocal manner. The metallic-nanosphere-on-aerogel structure ensures negligible distortion to the focal spots, low crosstalk between orthogonal polarization components (1/39 in experiment), and a low level background noise (1/80 of peak intensity in experiment), while high contrast imaging is not limited by the resonance bandwidth.

OCIS codes: (140.3295) Laser beam characterization; (170.5810) Scanning microscopy; (220.4241) Nanostructure fabrication; (260.5430) Polarization; (290.5850) Scattering, particles.

References and links

1. Q. Zhan, "Cylindrical vector beams: from mathematical concepts to applications," Adv. Opt. Photon. **1**(1), 1–57 (2009).
2. S. E. Skelton, M. Sergides, R. Saija, M. A. Iatì, O. M. Maragó, and P. H. Jones, "Trapping volume control in optical tweezers using cylindrical vector beams," Opt. Lett. **38**(1), 28–30 (2013).
3. Q. Zhan, "Trapping metallic Rayleigh particles with radial polarization," Opt. Express **12**(15), 3377–3382 (2004).
4. M. G. Donato, S. Vasi, R. Sayed, P. H. Jones, F. Bonaccorso, A. C. Ferrari, P. G. Gucciardi, and O. M. Maragò, "Optical trapping of nanotubes with cylindrical vector beams," Opt. Lett. **37**(16), 3381–3383 (2012).
5. O. M. Maragò, P. H. Jones, P. G. Gucciardi, G. Volpe, and A. C. Ferrari, "Optical trapping and manipulation of nanostructures," Nat. Nanotechnol. **8**(11), 807–819 (2013).
6. F. Peng, B. Yao, S. Yan, W. Zhao, and M. Lei, "Trapping of low-refractive-index particles with azimuthally polarized beam," J. Opt. Soc. Am. B **26**(12), 2242–2247 (2009).
7. Q. Zhan, "Trapping nanoparticles with cylindrical polarization," Proc. SPIE **5514**, 275–282 (2004).
8. J. R. Zurita-Sánchez and L. Novotny, "Multipolar interband absorption in a semiconductor quantum dot. II. Magnetic dipole enhancement," J. Opt. Soc. Am. B **19**(11), 2722–2726 (2002).
9. V. G. Niziev and A. V. Nesterov, "Influence of beam polarization on laser cutting efficiency," J. Phys. D Appl. Phys. **32**(13), 1455–1461 (1999).
10. M. Meier, V. Romano, and T. Feurer, "Material processing with pulsed radially and azimuthally polarized laser radiation," Appl. Phys., A Mater. Sci. Process. **86**(3), 329–334 (2007).
11. D. P. Biss, K. S. Youngworth, and T. G. Brown, "Dark-field imaging with cylindrical-vector beams," Appl. Opt. **45**(3), 470–479 (2006).
12. G. M. Lerman, A. Yanai, and U. Levy, "Demonstration of nanofocusing by the use of plasmonic lens illuminated with radially polarized light," Nano Lett. **9**(5), 2139–2143 (2009).
13. W. Chen, R. L. Nelson, D. C. Abeysinghe, and Q. Zhan, "Optimal plasmon focusing with spatial polarization engineering," Opt. Photon. News **20**(10), 36–41 (2009).
14. R. P. Zaccaria, F. De Angelis, A. Toma, L. Razzari, A. Alabastri, G. Das, C. Liberale, and E. Di Fabrizio, "Surface plasmon polariton compression through radially and linearly polarized source," Opt. Lett. **37**(4), 545–547 (2012).
15. D. Wang, T. Yang, and K. B. Crozier, "Optical antennas integrated with concentric ring gratings: electric field enhancement and directional radiation," Opt. Express **19**(3), 2148–2157 (2011).

#233042 - $15.00 USD Received 22 Jan 2015; revised 10 Mar 2015; accepted 15 Mar 2015; published 23 Mar 2015

16. B. Liu, D. Wang, C. Shi, K. B. Crozier, and T. Yang, "Vertical optical antennas integrated with spiral ring gratings for large local electric field enhancement and directional radiation," Opt. Express **19**(11), 10049–10056 (2011).
17. L. Du, D. Y. Lei, G. Yuan, H. Fang, X. Zhang, Q. Wang, D. Tang, C. Min, S. A. Maier, and X. Yuan, "Mapping plasmonic near-field profiles and interferences by surface-enhanced Raman scattering," Sci. Rep. **3**, 3064 (2013).
18. F. Lu, W. Zheng, and Z. Huang, "Coherent anti-Stokes Raman scattering microscopy using tightly focused radially polarized light," Opt. Lett. **34**(12), 1870–1872 (2009).
19. G. Terakado, K. Watanabe, and H. Kano, "Scanning confocal total internal reflection fluorescence microscopy by using radial polarization in the illumination system," Appl. Opt. **48**(6), 1114–1118 (2009).
20. H. Kang, B. Jia, J. Li, D. Morrish, and M. Gu, "Enhanced photothermal therapy assisted with gold nanorods using a radially polarized beam," Appl. Phys. Lett. **96**(6), 063702 (2010).
21. B. Jia, H. Kang, J. Li, and M. Gu, "Use of radially polarized beams in three-dimensional photonic crystal fabrication with the two-photon polymerization method," Opt. Lett. **34**(13), 1918–1920 (2009).
22. A. Bouhelier, M. Beversluis, A. Hartschuh, and L. Novotny, "Near-field second-harmonic generation induced by local field enhancement," Phys. Rev. Lett. **90**(1), 013903 (2003).
23. M. Beversluis, A. Bouhelier, and L. Novotny, "Continuum generation from single gold nanostructures through near-field mediated intraband transitions," Phys. Rev. B **68**(11), 115433 (2003).
24. X. Li, Y. Cao, and M. Gu, "Superresolution-focal-volume induced 3.0 Tbytes/disk capacity by focusing a radially polarized beam," Opt. Lett. **36**(13), 2510–2512 (2011).
25. P. Zijlstra, J. W. M. Chon, and M. Gu, "Five-dimensional optical recording mediated by surface plasmons in gold nanorods," Nature **459**(7245), 410–413 (2009).
26. J. Shu, Z. Chen, J. Pu, and Y. Liu, "Tight focusing of a double-ring-shaped, azimuthally polarized beam through a dielectric interface," J. Opt. Soc. Am. A **31**(6), 1180–1185 (2014).
27. H. Ye, C. Wan, K. Huang, T. Han, J. Teng, Y. S. Ping, and C. W. Qiu, "Creation of vectorial bottle-hollow beam using radially or azimuthally polarized light," Opt. Lett. **39**(3), 630–633 (2014).
28. L. Novotny and S. J. Stranick, "Near-field optical microscopy and spectroscopy with pointed probes," Annu. Rev. Phys. Chem. **57**(1), 303–331 (2006).
29. A. Bouhelier, M. R. Beversluis, and L. Novotny, "Near-field scattering of longitudinal fields," Appl. Phys. Lett. **82**(25), 4596 (2003).
30. E. Descrovi, L. Vaccaro, L. Aeschimann, W. Nakagawa, U. Staufer, and H. P. Herzig, "Optical properties of microfabricated fully-metal-coated near-field probes in collection mode," J. Opt. Soc. Am. A **22**(7), 1432–1441 (2005).
31. B. Jia, X. Gan, and M. Gu, "Direct observation of a pure focused evanescent field of a high numerical aperture objective lens by scanning near-field optical microscopy," Appl. Phys. Lett. **86**(13), 131110 (2005).
32. T. Grosjean, I. A. Ibrahim, M. A. Suarez, G. W. Burr, M. Mivelle, and D. Charraut, "Full vectorial imaging of electromagnetic light at subwavelength scale," Opt. Express **18**(6), 5809–5824 (2010).
33. S. V. Alferov, S. N. Khonina, and S. V. Karpeev, "Study of polarization properties of fiber-optics probes with use of a binary phase plate," J. Opt. Soc. Am. A **31**(4), 802–807 (2014).
34. Y. Zou, P. Steinvurzel, T. Yang, and K. B. Crozier, "Surface plasmon resonances of optical antenna atomic force microscope tips," Appl. Phys. Lett. **94**(17), 171107 (2009).
35. M. Mivelle, I. A. Ibrahim, F. Baida, G. W. Burr, D. Nedeljkovic, D. Charraut, J. Y. Rauch, R. Salut, and T. Grosjean, "Bowtie nano-aperture as interface between near-fields and a single-mode fiber," Opt. Express **18**(15), 15964–15974 (2010).
36. W. Bao, M. Melli, N. Caselli, F. Riboli, D. S. Wiersma, M. Staffaroni, H. Choo, D. F. Ogletree, S. Aloni, J. Bokor, S. Cabrini, F. Intonti, M. B. Salmeron, E. Yablonovitch, P. J. Schuck, and A. Weber-Bargioni, "Mapping local charge recombination heterogeneity by multidimensional nanospectroscopic imaging," Science **338**(6112), 1317–1321 (2012).
37. W. Bao, M. Staffaroni, J. Bokor, M. B. Salmeron, E. Yablonovitch, S. Cabrini, A. Weber-Bargioni, and P. J. Schuck, "Plasmonic near-field probes: a comparison of the campanile geometry with other sharp tips," Opt. Express **21**(7), 8166–8176 (2013).
38. K. G. Lee, H. W. Kihm, J. E. Kihm, W. J. Choi, H. Kim, C. Ropers, D. J. Park, Y. C. Yoon, S. B. Choi, D. H. Woo, J. Kim, B. Lee, Q. H. Park, C. Lienau, and D. S. Kim, "Vector field microscopic imaging of light," Nat. Photonics **1**(1), 53–56 (2007).
39. L. Novotny and N. van Hulst, "Antennas for light," Nat. Photonics **5**(2), 83–90 (2011).
40. T. Bauer, S. Orlov, U. Peschel, P. Banzer, and G. Leuchs, "Nanointerferometric amplitude and phase reconstruction of tightly focused vector beams," Nat. Photonics **8**(1), 23–27 (2013).
41. L. Novotny, M. R. Beversluis, K. S. Youngworth, and T. G. Brown, "Longitudinal field modes probed by single molecules," Phys. Rev. Lett. **86**(23), 5251–5254 (2001).
42. B. Hao and J. Leger, "Experimental measurement of longitudinal component in the vicinity of focused radially polarized beam," Opt. Express **15**(6), 3550–3556 (2007).
43. G. Kihara Rurimo, M. Schardt, S. Quabis, S. Malzer, C. Dotzler, A. Winkler, G. Leuchs, G. H. Döhler, D. Driscoll, M. Hanson, A. C. Gossard, and S. F. Pereira, "Using a quantum well heterostructure to study the longitudinal and transverse electric field components of a strongly focused laser beam," J. Appl. Phys. **100**(2), 023112 (2006).
44. K. G. Lee, H. W. Kihm, K. J. Ahn, J. S. Ahn, Y. D. Suh, C. Lienau, and D. S. Kim, "Vector field mapping of local polarization using gold nanoparticle functionalized tips: independence of the tip shape," Opt. Express **15**(23), 14993–15001 (2007).

#233042 - $15.00 USD Received 22 Jan 2015; revised 10 Mar 2015; accepted 15 Mar 2015; published 23 Mar 2015

45. T. Kalkbrenner, U. Håkanson, and V. Sandoghdar, "Tomographic plasmon spectroscopy of a single gold nanoparticle," Nano Lett. **4**(12), 2309–2314 (2004).
46. L. Novotny, R. D. Grober, and K. Karrai, "Reflected image of a strongly focused spot," Opt. Lett. **26**(11), 789–791 (2001).
47. L. Tong, J. Lou, R. R. Gattass, S. He, X. Chen, L. Liu, and E. Mazur, "Assembly of silica nanowires on silica aerogels for microphotonic devices," Nano Lett. **5**(2), 259–262 (2005).
48. L. Xiao, M. D. W. Grogan, S. G. Leon-Saval, R. Williams, R. England, W. J. Wadsworth, and T. A. Birks, "Tapered fibers embedded in silica aerogel," Opt. Lett. **34**(18), 2724–2726 (2009).
49. L. Novotny and B. Hecht, "Dipole emission near planar interfaces," in *Principles of Nano-Optics* (Cambridge University, 2006), pp. 335–360.
50. T. Yang and K. B. Crozier, "Dispersion and extinction of surface plasmons in an array of gold nanoparticle chains: influence of the air/glass interface," Opt. Express **16**(12), 8570–8580 (2008).
51. E. Wolf, "Electromagnetic diffraction in optical systems. I. An integral representation of the image field," Proc. R. Soc. Lond. A Math. Phys. Sci. **253**(1274), 349–357 (1959).
52. B. Richards and E. Wolf, "Electromagnetic diffraction in optical systems. II. Structure of the image field in an aplanatic system," Proc. R. Soc. Lond. A Math. Phys. Sci. **253**(1274), 358–379 (1959).
53. L. Novotny and B. Hecht, "Propagation and focusing of optical fields," in *Principles of Nano-Optics* (Cambridge University, 2006), pp. 45–86.
54. R. Dorn, S. Quabis, and G. Leuchs, "The focus of light-linear polarization breaks the rotational symmetry of the focal spot," J. Mod. Opt. **50**(12), 1917–1926 (2003).
55. V. V. Kotlyar, S. S. Stafeev, Y. Liu, L. O'Faolain, and A. A. Kovalev, "Analysis of the shape of a subwavelength focal spot for the linearly polarized light," Appl. Opt. **52**(3), 330–339 (2013).
56. H. Gersen, L. Novotny, L. Kuipers, and N. F. van Hulst, "On the concept of imaging nanoscale vector fields," Nat. Photonics **1**(5), 242 (2007).

1. Introduction

When a laser beam is focused under high numerical aperture (NA), the vectorial profile of the focal spot can be manipulated to achieve a lot of intriguing light-matter interactions [1]. A wide range of applications have been explored, which include optical trapping [2–7], laser cutting and drilling [8–10], optical imaging [11], surface plasmon excitation and focusing [12–16], Raman scattering [17,18], fluorescence [19], photothermal therapy [20], two photon absorption lithography [21], harmonics generation [22,23], optical data storage [24,25], unique beam shaping [26,27], etc. To obtain knowledge of the vectorial profiles of the focal spots, a variety of characterization methods have been demonstrated, which include scanning near-field optical microscopy (SNOM) [28–33], optical antennas [34,35], a campanile nanofocusing geometry [36,37], metallic nanoparticle scattering [38–40], molecular absorption [41], exposing photoresist [42], anisotropic absorption of quantum wells [43], and mathematical reconstruction [32,40].

Among the above mentioned vectorial profiling methods, scanning a metallic nanosphere across the focal spot has been proposed to replace the complicated SNOM technique, and to obtain more than a single polarization component. Bauer et al. have recently demonstrated full-vectorial profiling results which very closely replicate the theoretical predictions, by reconstructing both the amplitude and the phase of the field vectors from the Mie scattering interference patterns of a metallic nanosphere [40]. However, in general, reconstruction requires a stable optical alignment within the measurement time. When there is mechanical drift which is difficult to avoid in many experiments, or when the focal spot is not perfect and contains high order spherical harmonics, a direct measurement shall be useful. Earlier, Lee et al. have reported direct measurement results by scanning a fiber taper functionalized with a metallic nanosphere [38,39]. In their experiment, the polarizability tensor was measured to distinguish the contribution from different polarization components [44], which was reported to vary a lot between different probes [45]. The significant variation between and the anisotropicity of the metallic nanosphere functionalized fiber probes are inherent in the method itself, due to the nanosphere-fiber interface, as will be explained later in this paper. Another important concern with focal spot profiling is that whenever the scanning scatter is sitting on a substrate, e.g. an antenna sitting on a SNOM probe, or a nanoparticle sitting on a fiber taper, the substrate distorts the focal spot and induces significant aberration under high NA focusing [46].

In this paper, we report direct measurement of the focal spots' vectorial profiles by employing a metallic nanosphere supported on an aerogel substrate as the scanning probe.

#233042 - $15.00 USD Received 22 Jan 2015; revised 10 Mar 2015; accepted 15 Mar 2015; published 23 Mar 2015

The three orthogonal electric field components in the focal spots are measured by monitoring the nanosphere's far-field scattering along the corresponding polarizations. Due to the aerogel substrate's close-to-unity refractive index, the nanosphere probe has an isotropic polarizability, and the focal spot profile is not distorted by the substrate. The profiling results of He-Ne laser focal spots in three different polarization states are reported, which show a high signal-to-background ratio (SBR) and a high cross-polarization suppression ratio (CPSR) even when the laser wavelength is off the surface plasmon resonance of the nanosphere, and without using lock-in detection which is commonly adopted by SNOM experiments.

2. The scanning probe: a metallic nanosphere on an aerogel substrate

We use a 100 nm diameter gold nanosphere on a silica aerogel substrate as the scanning probe. Aerogel is a porous nano material with typically more than 95% of its volume filled with air, which leads to an extremely low density and a refractive index almost equal to that of air, yet it is mechanically solid. It has been used by optics researchers to support microphotonic devices without introducing modification to light propagation behavior [47,48]. In our work, the aerogel substrate is used to "suspend" the gold nanosphere in air, so that modification to the focal spot profile by the substrate is negligible. The sample was prepared by putting a droplet of 100 nm diameter gold nanosphere colloid (TedPella), which had been diluted and contained around 10^8 nanospheres per milliliter, on the silica aerogel substrate. After being dried under ambient conditions for about an hour, the sample was rinsed with water and blown dry with a nitrogen gun. In Fig. 1, a broadband light beam from a halogen lamp is focused by a microscope objective with NA = 0.55 into the aerogel substrate. The outline of the focused beam can be viewed due to weak scattering off the porous nanostructure.

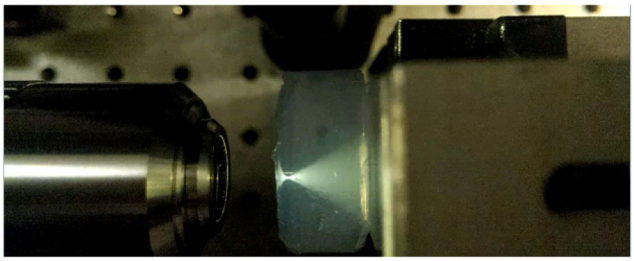

Fig. 1. A broadband light beam focused into a silica aerogel substrate. The NA of the microscope objective is 0.55.

Another reason for using the aerogel substrate is that it doesn't influence the scattering cross section of the gold nanosphere on top of it, so as for the nanosphere to be an isotropic scattering probe. This is critical for simultaneous profiling of all polarization components, in contrast to optical antennas that rely upon dominant scattering along one of the polarizations. To illustrate the substrate influence, the calculated scattering spectra of a 100 nm diameter gold nanosphere in air and on a glass substrate are compared in Fig. 2, which shows significant difference between s-wave (normal) and p-wave illumination. When the oscillating dipole of the nanosphere on a glass substrate is parallel to the surface of the substrate, since the electric field has little overlap with the substrate, the scattering cross section is almost the same as that in air. But when the oscillating dipole of the nanosphere is normal to the surface of the substrate, its scattering cross section at relatively longer wavelengths is significantly increased. In addition, dipoles with different orientations on a glass substrate have quite different radiation behaviors [49,50]. These two factors contribute to large anisotropicity and off-diagonal elements in the polarizability matrix. Therefore, if a fiber taper functionalized with a metallic nanosphere is used as the scattering probe, the nanosphere-fiber interface's area and orientation will both have significant influence on the measurement result. The above calculation was done by using the total-field-scattered-field formulation of the finite-difference-time-domain (FDTD) method. In the simulation, the source was a pulse of

#233042 - $15.00 USD Received 22 Jan 2015; revised 10 Mar 2015; accepted 15 Mar 2015; published 23 Mar 2015

planewave and the boundary condition was perfectly matched layer. The grid size was 0.25 nm around the interface between the nanosphere and the substrate, and 5 to 10 nm elsewhere.

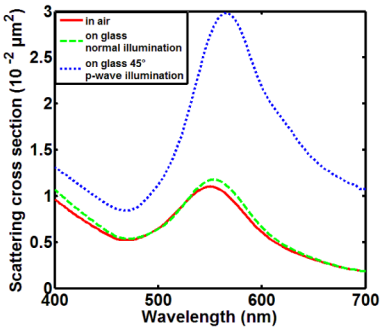

Fig. 2. Calculated scattering cross section of a 100 nm diameter gold nanosphere when it is in air, on top of a glass substrate under normal illumination, and on top of a glass substrate under 45°-to-normal p-wave illumination.

A typical experimental scattering spectrum of a single 100 nm gold nanosphere on the silica aerogel substrate is shown in Fig. 3, under the broadband illumination as shown in Fig. 1. The theoretical scattering spectrum in air which is extracted from Fig. 2 is also included for comparison. The broader bandwidth of the experimental result is largely due to the chromatic aberration of the focusing objective and the mean free path limitation of conduction electrons which has not been considered in the calculation. In addition, with very weak background scattering from the aerogel, we are not limited by the resonance bandwidth of the nanosphere to achieve a high SBR in our experiment. In the following demonstration, we used a He-Ne laser at 632.8 nm, which is almost off the resonance as in Fig. 3.

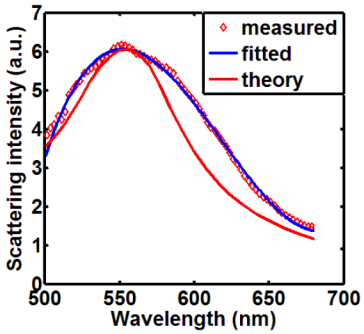

Fig. 3. Experimental scattering spectrum of a 100 nm diameter gold nanosphere on the silica aerogel substrate. The diamonds are measured scattering intensity, and the blue solid curve is a 3rd degree polynomial fitting. The scattering spectrum has been normalized to the spectrum of the incident beam. The theoretical scattering spectrum in air is extracted from Fig. 2 and included for comparison.

3. Scanning metallic nanosphere microscopy

The optical experiment setup is shown in Fig. 4. It consists of three parts: (1) generation of a He-Ne laser beam with different states of polarization, (2) a home-built optical microscope which focuses the laser beam, and which takes a bright field image of the metallic nanosphere, and (3) collection and confocal detection of the scanning nanosphere's far-field scattering along respective polarization directions.

#233042 - $15.00 USD Received 22 Jan 2015; revised 10 Mar 2015; accepted 15 Mar 2015; published 23 Mar 2015

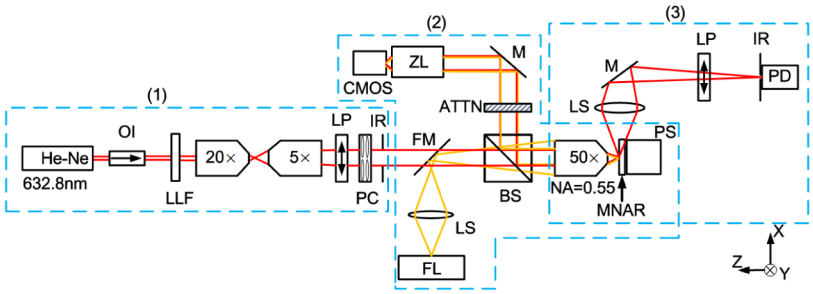

Fig. 4. Optical experiment setup. It consists of (1) a He-Ne laser beam converted to different states of polarization, (2) a home-built optical microscope, and (3) a scanning metallic nanosphere microscopy system. He-Ne, a He-Ne laser at 632.8 nm; OI, optical isolator; LLF, laser line filter; 20′, 20′ objective; 5′, 5′ objective; LP, linear polarizer; PC, liquid crystal polarization converter; IR, iris; FM, flip mirror; FL, fiber lamp; LS, lens; BS, 50-50% beam splitter; ATTN, attenuator; M, mirror; ZL, zoom lens; CMOS, CMOS camera; 50′, 50′ objective; MNAR, a metallic nanosphere on an aerogel substrate; PS, piezostage; PD, photodetector. The red and yellow lines indicate the flow of light from the laser and the fiber lamp, respectively.

In part (1), a He-Ne laser beam in the TEM_{00} mode is expanded by a pair of objectives, in order to fill the input aperture of the 50′ objective (in part (2)) for high NA focusing. Then the linearly polarized (LP) laser beam is converted to azimuthally polarized (AP) and radially polarized (RP) states by a polarization converter (ARCoptix). The polarization converter includes a twisted nematic liquid crystal cell, whose entrance plane and exit plane are linearly and circularly rubbed, respectively. When a linearly polarized light beam propagates through the liquid crystal, its spatial polarization follows the rotation of the liquid crystal and is converted to the desired state of polarization. Imperfect alignment between the laser beam and the liquid crystal cell induces observable distortion to the laser beam and its focal spot, which is believed to be a major cause for the difference between experimental results and theoretical predictions. The beam profile is cleaned up with an iris at the end of part (1). In part (2), the laser beam in its designated state of polarization is focused onto the metallic nanosphere through a 50′ objective, which has a NA of 0.55. A home-built microscope is used to obtain a bright field image of the nanosphere, so that we know the nanosphere is in the focal plane. In part (3), the metallic nanosphere on an aerogel substrate is raster scanned by a closed-loop piezoelectric stage. Far-field scattering off the nanosphere to the *x*-side direction is collected by a lens with NA = 0.3. The collected scattering power is measured with a simple confocal setup to block scattering from inside the aerogel, that is, the far-field is spatially filtered by an iris on the image plane of the collection lens and detected by a photodiode right behind the iris. Orthogonal polarization components can be distinguished by a linear polarizer before the iris. The nanosphere is placed close to the collecting lens' focal point so that the collected field is almost normally incident onto the polarizer (Fig. 4 is not drawn to scale).

The scanning metallic nanosphere microscopy works simply as follows. In order to measure the *z*-component of the electric field, E_z, of the laser focal spot, we scan the nanosphere across the laser's focal plane and detect the far-field scattering power in the *z* polarization. The same applies to E_y. For measuring E_x, a collecting lens on the *y*-side should be used. For simultaneous detection of all polarization components, two collecting lenses and three polarizers are needed, which are not shown in Fig. 4. For a perfect isotropic scatterer, the crosstalk between orthogonal polarizations increases with the collecting lens' NA, as shown in Fig. 5. The CPSR value in the figure is defined as follows: assuming the polarizer is in the *y*-direction, *y*-over-*z*(or *x*) CPSR = collected far-field scattering power when the radiating dipole is in the *y*-direction / collected far-field scattering power when the radiating dipole is in the *z*(or *x*)-direction. In our case, with a NA = 0.3 collecting lens, the *y*-over-*z* CPSR is $8.7′10^3$, and *y*-over-*x* CPSR is 38, which are theoretical limits to experiment results.

#233042 - $15.00 USD Received 22 Jan 2015; revised 10 Mar 2015; accepted 15 Mar 2015; published 23 Mar 2015

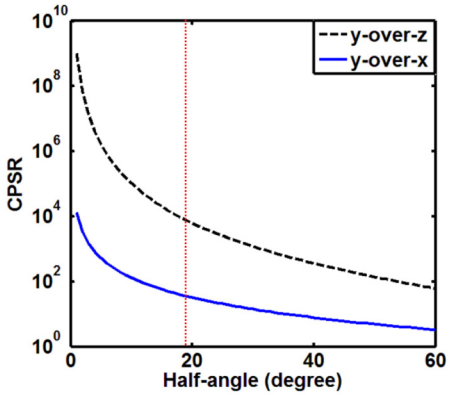

Fig. 5. Cross polarization suppression ratio (CPSR) versus half collection angle. The dotted red line corresponds to the collecting lens in our experiment.

Figure 5 has been calculated by deriving the mathematical expression of the far-field radiation of a linearly polarized dipole after being collimated by a collection lens, as following. A right-handed coordinate system is used. Both $\vec{r}$ and (x, y, z) are used to refer to a spatial point. $\hat{r}$ refers to a unit vector along $\vec{r}$, and so on. Here we assume that the radiating dipole is a point dipole sitting at the origin; the collection lens is in the y-z plane and has an infinitesimal thickness, with its center at $(f, 0, 0)$, where f is its focal distance. The well-known point dipole's radiation field just before the collection lens is defined as $\vec{E}(\vec{r})$, where $\vec{r}$ is a point on the plane of lens, that is, where the dipole radiation hits the lens. The plane of incidence (POI) is defined as the plane that contains the x-axis and the point $\vec{r}$. In order to calculate the electric field right after the collection lens, $\vec{E}_a(\vec{r})$, we decompose $\vec{E}(\vec{r})$ into its projections onto the POI, $\vec{E}_{POI}(\vec{r})$, and onto the surface norm of POI, $\vec{E}_{POI\_Norm}(\vec{r})$. Both $\vec{E}_{POI}(\vec{r})$ and $\vec{E}_{POI\_Norm}(\vec{r})$ will follow the rotation of the wave vector from $\hat{r}$ to $\hat{x}$ after going through the lens, but in different manners, to $\vec{E}_{a,POI}(\vec{r})$ and $\vec{E}_{a,POI\_Norm}(\vec{r})$, respectively. When $x, y, z \geq 0$, we have the following equations, and the collimated $\vec{E}_a(\vec{r})$ field is subsequently filtered by the polarizer and reaches the detector.

$$\vec{E}_a(\vec{r}) = \vec{E}_{a,POI}(\vec{r}) + \vec{E}_{a,POI\_Norm}(\vec{r}), \tag{1}$$

$$\vec{E}_{a,POI}(\vec{r}) = -\vec{E}(\vec{r}) \cdot \frac{\hat{x} - \hat{r}(\hat{r}\cdot\hat{x})}{\left|\hat{x} - \hat{r}(\hat{r}\cdot\hat{x})\right|} \frac{\hat{r} - \hat{x}(\hat{r}\cdot\hat{x})}{\left|\hat{r} - \hat{x}(\hat{r}\cdot\hat{x})\right|}, \tag{2}$$

$$\vec{E}_{a,POI\_Norm}(\vec{r}) = \vec{E}(\vec{r}) \cdot \frac{\hat{x}\times\hat{r}}{\left|\hat{x}\times\hat{r}\right|} \frac{\hat{x}\times\hat{r}}{\left|\hat{x}\times\hat{r}\right|}. \tag{3}$$

4. Vectorial profiling of focal spots

In this section, we describe the profiling results on the focal spots of AP, RP and LP He-Ne laser beams, using the scanning metallic nanosphere microscopy method introduced in the last two sections.

The AP polarization state refers to a cylindrical beam in which the electric field is polarized in the azimuthal direction, as shown in Fig. 6a. By the Richards-Wolf vectorial diffraction theory, at its focal plane, the electric field is polarized along the azimuthal direction in a doughnut shape [51,52]. For an AP focal spot in the x-y plane (please refer to Fig. 4 for the definition of the Cartesian coordinate system), we have calculated its $|E_y|^2$ and

#233042 - $15.00 USD Received 22 Jan 2015; revised 10 Mar 2015; accepted 15 Mar 2015; published 23 Mar 2015

$|E_z|^2$ profiles as shown in Figs. 6b&c, the latter being completely dark. The $|E_x|^2$ profile is just a 90° rotation of the $|E_y|^2$ profile and therefore not plotted or experimentally measured. The calculation followed Ref [53], using NA = 0.55.

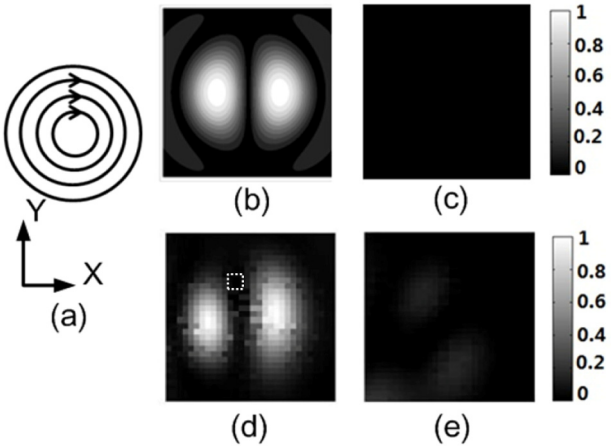

Fig. 6. The theoretical and experimental vectorial profiles of an azimuthally polarized (AP) focal spot. (a) A schematic of the electric field in a collimated AP laser beam. (b) Theoretical $|E_y|^2$ profile. (c) Theoretical $|E_z|^2$ profile. (d) Experimental $|E_y|^2$ profile. (e) Experimental $|E_z|^2$ profile. All images are 2.4´2.4 μm^2. Laser wavelength is 632.8 nm, focusing NA = 0.55.

Experimental profiling has been done by using a He-Ne laser and raster scanning a 100 nm gold nanosphere on the aerogel substrate in the focal plane, at a step of 80 nm. The profiling results of $|E_y|^2$ and $|E_z|^2$ are shown in Figs. 6d&e, respectively. An SBR value of 80 is obtained. The non-zero $|E_z|^2$ profile is mainly due to the aberration in the collimated laser beam as could be clearly viewed in our experiment, and the measured focal spot shape has also been influenced by the mechanical drift of the stage supporting the aerogel. Limited by the quality of the focal spot in our experiment, instead of drawing a line trace plot to compare the theoretical and experimental data quantitatively, we choose a dashed box in Fig. 6d which approximately corresponds to where $|E_x|^2$ is the highest but blocked by the polarizer. By comparing the dashed box to the highest intensity in the same figure, after subtracting the background noise of 1/80 according to the experimental SBR value, we obtained an experimental *y*-over-*x* CPSR value of 39, which agrees well with the theoretical limit for a perfectly isotropic scatterer. The experimental CPSR value is not as small at all spatial points, which could either result from the aberration of the focal spot, or limited by the ellipticity of the nanosphere.

Similarly, the profiling results on the focal spot of the RP He-Ne laser beam are shown in Fig. 7, which is longitudinally polarized at the center of the focal spot.

#233042 - $15.00 USD Received 22 Jan 2015; revised 10 Mar 2015; accepted 15 Mar 2015; published 23 Mar 2015

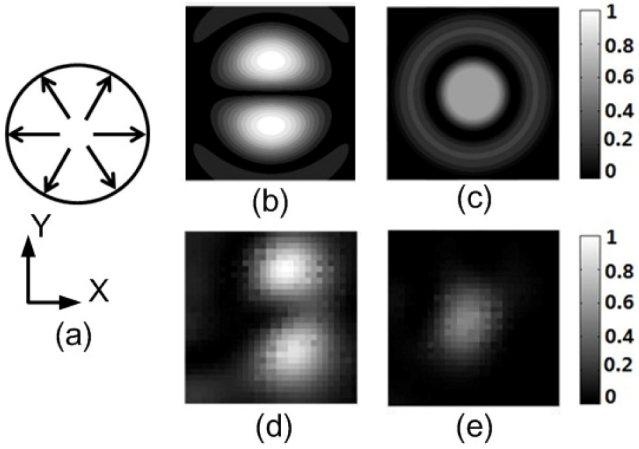

Fig. 7. The theoretical and experimental vectorial profiles of a radially polarized (RP) focal spot. (a) A schematic of the electric field in a collimated RP laser beam. (b) Theoretical $|E_y|^2$ profile. (c) Theoretical $|E_z|^2$ profile. (d) Experimental $|E_y|^2$ profile. (e) Experimental $|E_z|^2$ profile. All images are 2.4´2.4 μm^2. Laser wavelength is 632.8 nm, focusing NA = 0.55.

The focal spot of the "conventional" LP He-Ne laser beam has also been characterized, with a focusing NA of 0.9 and a scanning step of 50 nm, as shown in Fig. 8. Its linear polarization breaks the rotational symmetry and results in an elliptical intensity profile under high NA focusing [54,55]. The experimental results have been normalized by taking the peak intensity to be the same as the theoretical predictions, for both $|E_y|^2$ and $|E_z|^2$. The weak $|E_x|^2$ profile has a theoretical maximum of 0.014, and is smeared out by aberration and background noise in the experiment, which is not plotted. The dashed box in Fig. 8e approximately corresponds to where $|E_y|^2$ is the highest but blocked by the polarizer. By comparing it to the highest intensity in Fig. 8d, after subtracting a nominal background noise of 1/80, we obtained an experimental *y*-over-*z* CPSR value of around 260, which is much higher than the *y*-over-*x* CPSR value as have been predicted by the theoretical work in the last section. Line trace plots are also shown in Fig. 8f to compare the theoretical and experimental data.

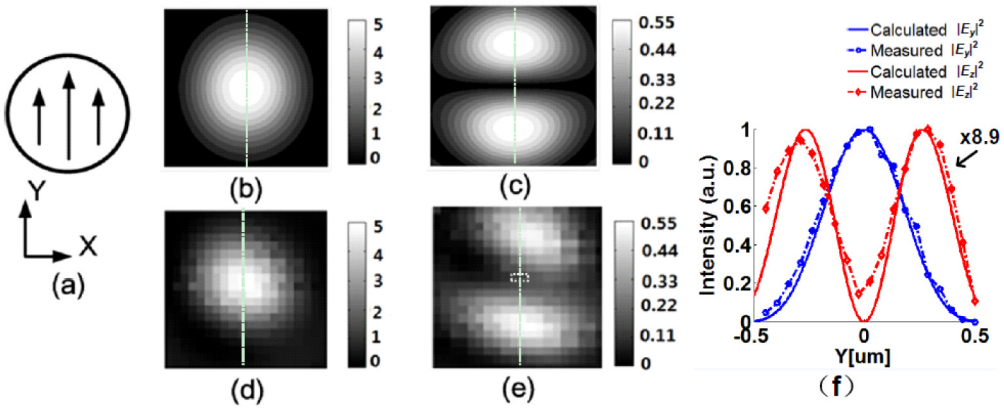

Fig. 8. The theoretical and experimental vectorial profiles of a linearly polarized (LP) focal spot. (a) A schematic of the electric field in a collimated LP laser beam. (b) Theoretical $|E_y|^2$ profile. (c) Theoretical $|E_z|^2$ profile. (d) Experimental $|E_y|^2$ profile. (e) Experimental $|E_z|^2$ profile. (f) Line trace plots along the dashed lines in (b) through (e), the $|E_z|^2$ curves have been multiplied by a factor of 8.9. All images are 1´1 μm^2. Laser wavelength is 632.8 nm, focusing NA = 0.9.

#233042 - $15.00 USD Received 22 Jan 2015; revised 10 Mar 2015; accepted 15 Mar 2015; published 23 Mar 2015

5. Conclusion

We have demonstrated a vectorial, broadband, high contrast and subwavelength resolution method for laser focal spots' direct profiling. By scanning a 100 nm diameter gold nanosphere on a silica aerogel substrate in the focal plane of a He-Ne laser beam, and measuring its far-field scattering by confocal detection, a CPSR of 39 and an SBR of 80 have been experimentally obtained without resorting to resonance. Our method is better than the popular SNOM measurement in that the low refractive index of aerogel enables simultaneous and isotropic measurement of different polarization components with little crosstalk, and avoids focal spot distortion. The theoretical limit of CPSR by using a collecting lens has also been calculated.

It is worth mentioning that since any two polarization components can be detected using the same collecting lens, by adding a 45° linear polarizer and a circular polarizer, the Stokes vector and the relative phase between the orthogonal polarization components can be obtained, which is not included in this work. This phase information has been pointed out to be a key element for "full-vectorial" profiling [56]. It could also be worth discussing that since the oscillating dipole of the nanosphere is only induced by the local field, the profiling resolution is expected to be limited by the size of the nanosphere only and will not be compromised by the resonance enhanced scattering cross section. However, as the Rayleigh scattering cross section decreases as the sixth power of nanosphere diameter, there is a tradeoff between spatial resolution, resonance bandwidth and signal-to-noise ratio.

Acknowledgments

This work is supported by the National Science Foundation of China under grant # 11204177 and # 61275168, the Research Fund for the Doctoral Program of Higher Education of China under grant # 20120073110050, and the Fundamental Research Program of Science and Technology Commission of Shanghai Municipality under grant # 14JC1491700.